Shock/bubble interaction near a rigid boundary in shock wave lithotripsy

A.R. Jamaluddin[1], G.J. Ball[2], and T.G. Leighton[3]

[1] *School of Engineering Sciences, University of Southampton, Highfield, SO17 1BJ, UK*
[2] *Atomic Weapons Establishment, Aldermaston, Reading, RG7 4PR, UK*
[3] *Inst. of Sound and Vibration Research, University of Southampton, Highfield, SO17 1BJ, UK*

Abstract. A Free-Lagrange CFD code is used to model in axisymmetric form the near-field interactions between a lithotripter shock wave and a single spherical air bubble near a rigid boundary in water. The asymmetric collapse of the bubble is induced by the relatively strong incident lithotripter shock wave, and influenced by the presence of the rigid boundary in the vicinity of the bubble. These two factors are contributory elements to a full description of the bubble collapse processes. The bubble collapses and undergoes jetting, which consequently generates a blast wave into the surrounding water owing to a liquid-liquid impact. Following impact, the bubble attains a toroidal shape and undergoes subsequent expansion. A detailed description of the shock/bubble interaction event is given, which includes the primary collapse and pressure-time histories on the rigid boundary.

1 Introduction

Studies of Extracorporeal Shock Wave Lithotripsy (ESWL) have shown that cavitation bubbles are induced *in vivo* near the lithotripter focus by the tensile stress of the lithotripter shock wave pulses [1]. The collapse of such cavitation bubbles near a solid surface [2] or by an incident shock [3] can produce a liquid jet. The mechanical stresses generated by the shock-bubble interaction and subsequent jet impact on the kidney stone have been identified as a possible mechanism of stone fragmentation during lithotripsy [4]. However, the violent collapse of cavitation bubbles also causes collateral damage to the kidneys as well as the surrounding tissue [5]. The costs and benefits of the treatment are therefore highly dependent on whether the focal point of the lithotripter generator is accurately targeted on the stone.

Despite these findings, current commercial lithotripters are not equipped with any means to assess qualitatively the cavitation activity in patients during clinical lithotripsy. One means of detecting the presence of cavitation bubbles is to measure their acoustic emissions [6,7]. In an attempt to explore the feasibility of assessing inertial cavitation *in vivo* during SWL based on acoustic measurements, Zhong *et al.* [8] studied the dynamics of cavitation *in vitro* using high-speed photography. They measured the associated acoustic emission in water emanating from the focus of an electrohydraulic shock wave lithotripter. A clear correlation between the dynamics of lithotripsy-induced cavitation bubbles and the resultant acoustic emission was identified. Cunningham *et al.* [7] used time-frequency analysis to quantify cavitation activity *in vivo*, and used the time of the detected acoustic emissions to infer a value for the radius of secondary stable bubbles[1]. However, in most experimental work, understanding of the fluid mechanics involved is incomplete owing to the limited temporal and spatial resolution of available experimental diagnostics.

The main objective of the present work is to simulate shock-induced bubble collapse by lithotripter shock waves using the Free-Lagrange method in axisymmetric form, and to predict the resulting acoustic emission in the near field.

[1] A secondary stable bubble is a bubble which has been formed as a result of the interaction of a preceding lithotripter pulse with a cavitation nucleus, and which has reached a state of mechanical equilibrium with the surrounding fluid.

2 Numerical method

The numerical simulation is performed using the Free-Lagrange (FL) code, *Vucalm*, developed by Ball [9]. The code solves the unsteady, inviscid and compressible Euler equations in either two-dimensional or axi-symmetric form. The flow solver is of Godunov-type, and nominal 2^{nd} order spatial accuracy is achieved using a piece-wise linear reconstruction of conserved variables. In order to ensure monotonicity at steep gradients, a slope limiter based on the MUSCL approach is used.

The FL method uses a fully unstructured Lagrangian mesh in which the connectivity is allowed to change freely as the flow evolves, and is thereby suitable for highly deforming flows. The working fluid is divided into discrete polygonal cells, each containing a single particle which carries information of fluid type, properties, coordinates and flow conditions. The locations of the cell boundaries are determined by constructing a Voronoi mesh. The mass and fluid type of each mesh cell is assigned from the start of the simulation and never changes. There are no mixed cells and hence the material interfaces are always sharply resolved; interface tracking or reconstruction algorithms are not required. The code employs a simple interface smoothing algorithm which acts as a form of artificial surface tension [10]. This prevents numerically seeded Richtmyer-Meshkov instability occurring on the the interface when it is strongly shocked. Water is represented by the Tait equation of state, while the ideal gas equation is used for air. The code uses the HLLC approximate Riemann solver at gas/gas interfaces and an exact solver at gas/water and water/water cell interfaces [11].

3 Problem specification

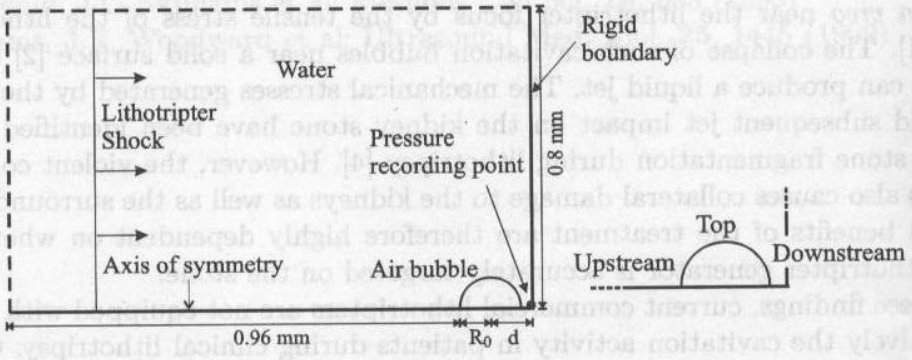

Fig. 1. The geometry of the problem (not to scale) and bubble surface name convention

The problem studied in the present work comprises a single spherical air bubble near a rigid boundary immersed in water (Fig. 1). The initial density for air and water are $1.2246\,kgm^{-3}$ and $1000\,kgm^{-3}$ respectively while the initial temperature and pressure for both fluids are $0.1\,MPa$ and $288.15\,K$. The initial air bubble radius $R_0 = 0.04\,mm$ [7], which was chosen to be typical of a secondary stable bubble, and d is the distance from the initial bubble centre to the rigid boundary. Here, the *stand-off parameter*, $\zeta = \frac{d}{R_0}$, is 1.0625.

The lithotripter pulse is introduced by imposing a time-dependent pressure boundary condition on the left boundary. The idealised lithotripter shock profile consists of a leading shock front with peak positive pressure, $P^+ = 50\,MPa$, followed by a tensile wave with a peak negative pressure, $P^- = -10\,MPa$, and a total pulse duration of 3 to $7\,\mu s$ [12]. The shock propagates through the water from left to right. The top boundary is non-reflecting at all times. A pressure recording point is positioned at the rigid boundary on the axis of symmetry, a distance d from the initial bubble centre in order to register pressure pulses produced by cavitation events. A mesh of approximately $35{\times}10^3$ cells has been used. All elapsed times are measured from the first

shock/bubble impact. The gas is modelled as air and is represented by the Ideal Gas Equation (EOS). The water is represented by the Tait Equation of state.

4 Results and discussion

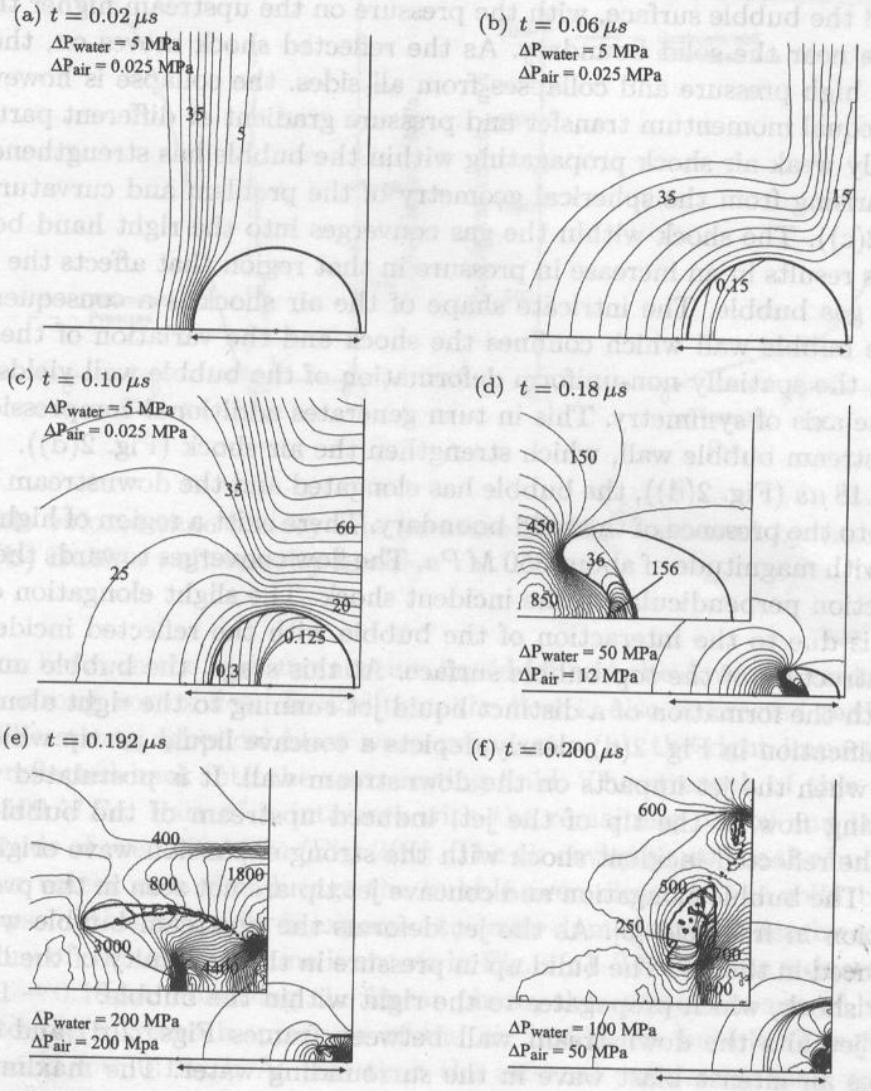

Fig. 2. Pressure contours of a bubble with initial radius $R_0 = 40\,\mu m$ collapsed by a lithotripter shock wave with strength of $P^+ = 50\,MPa$. Horizontal arrows indicate initial size and position of bubble

The results of the shock/bubble interaction are shown in Fig. 2. Fig. 2(a) is $0.02\,\mu s$ after the shock first impacts the bubble wall. As a result of the large difference in acoustic impedance between the air and water, when the lithotripter shock wave strikes the upstream bubble wall a weak shock is transmitted into the air and a strong expansion wave is generated in the surrounding water that propagates leftwards and upwards. The particle velocity behind the shock is high, and therefore a large momentum impacts the gas-water interface. This causes the bubble wall to deform to the right.

The interaction between the incident lithotripter shock and the expansion waves originating at the bubble surface results in significant weakening and curvature of the shock. At $t = 0.06\,\mu s$ (Fig. 2(b)), the incident shock has traversed the full bubble width and impacts on the nearby

solid boundary. The reflected shock then interacts with the expansion wave and is weakened further. At this time, the top of the interface starts to collapse. The shock which has been transmitted into the air bubble propagates more slowly and decouples from the incident shock, while the bubble wall continues to deform.

The pressure gradient in the water near the upstream of the bubble increases as time progresses (Fig. 2(c)). The pressure gradients drive the particles to flow toward the bubble. Further interaction with the reflected incident shock leads to an increasingly non-uniform pressure distribution around the bubble surface, with the pressure on the upstream higher than that on the downstream side near the solid boundary. As the reflected shock moves on, the whole bubble is enclosed by a high pressure and collapses from all sides. the collapse is however asymmetric owing to the unequal momentum transfer and pressure gradient at different parts of the bubble wall. The initially weak air shock propagating within the bubble has strengthened owing to the focusing effect arising from the spherical geometry of the problem and curvature of the bubble interface (Fig. 2(c)). The shock within the gas converges into the right hand bottom corner of the bubble. This results in an increase in pressure in that region that affects the direction of the flow within the gas bubble. The intricate shape of the air shock is a consequence of both the geometry of the bubble wall which confines the shock and the variation of the geometry with time. Moreover, the spatially non-uniform deformation of the bubble wall yields a higher water velocity near the axis of symmetry. This in turn generates additional compression waves in the air near the upstream bubble wall, which strengthen the air shock (Fig. 2(d)).

When $t = 0.18\,\mu s$ (Fig. 2(d)), the bubble has elongated and the downstream bubble wall has flattened owing to the presence of the solid boundary. There exist a region of high pressure on the upstream wall with magnitude of about $850\,MPa$. The flow converges towards the rigid boundary and in the direction perpendicular to the incident shock. The slight elongation of bubble in the axial direction is due to the interaction of the bubble with the reflected incident shock which induces the contraction of the top bubble surface. At this stage, the bubble undergoes a rapid deformation with the formation of a distinct liquid jet running to the right along the symmetry axis. The magnification in Fig. 2(d) clearly depicts a concave liquid jet tip which might results in trapped gas when the jet impacts on the downstream wall. It is postulated that this results from a circulating flow at the tip of the jet, induced upstream of the bubble wall from the interaction of the reflected incident shock with the strong expansion wave originating from the bubble surface. The bubble elongation and concave jet tip are not seen in the problem for shock-bubble interaction in free-field [3]. As the jet deforms the upstream bubble wall, compression waves are produced in the air. The build up in pressure in the proximity of the liquid jet induces a secondary air shock, which propagates to the right within the bubble.

The liquid jet hits the downstream wall between frames Figs. 2(d) and (e). On impact, the jet produces an intense blast wave in the surrounding water. The maximum effect of the blast wave is localised at the point of liquid-liquid impact and the peak over-pressure decays rapidly with distance from the jet impact point. The peak pressure loading registered on the rigid boundary is nearly $7000\,MPa$ (Fig. 3(b)). At $t = 0.192\,\mu s$, the jet has penetrated through the bubble, isolating a lobe of trapped air and highly compressed gas which form a toroid in three dimensions (Fig. 2(e)). The jet continues to accelerate as it pierces the bubble, reaching a maximum speed of over $2000\,ms^{-1}$ immediately prior to jet impact (Fig. 3(b)). It is believed that high-speed jets of this type play a primary role in cavitation erosion as well as formation of circular pits and indentation on metal foils [1]. In comparison to the upstream wall velocity, the velocity achieved by the downstream wall is very small and the flow in that region appears to stagnate.

The jet impact also leads to the creation of bubble fragments originating from the air layer trapped between the jet tip and the downstream interface prior to impact. This is probably a numerical artefact, although it is likely that a qualitatively similar effect could occur in reality. However, it is very difficult to quantify experimentally owing to the very small length and time scales of the problem. If such tiny isolated islands of gas do exist, they may coalesce with the main cavity as the flow evolves, act as nuclei for further cavitation events or diffuses into

the water. The interaction of these nuclei with the tensile part of the lithotripter shock wave will cause them to expand and collapse, either spherically or asymmetrically, depending on the nature of the flow around the bubble and the degree of influence of the nearby solid boundary. These bubble fragments could also be collapsed by shock waves emitted from the collapse of neighbouring bubbles.

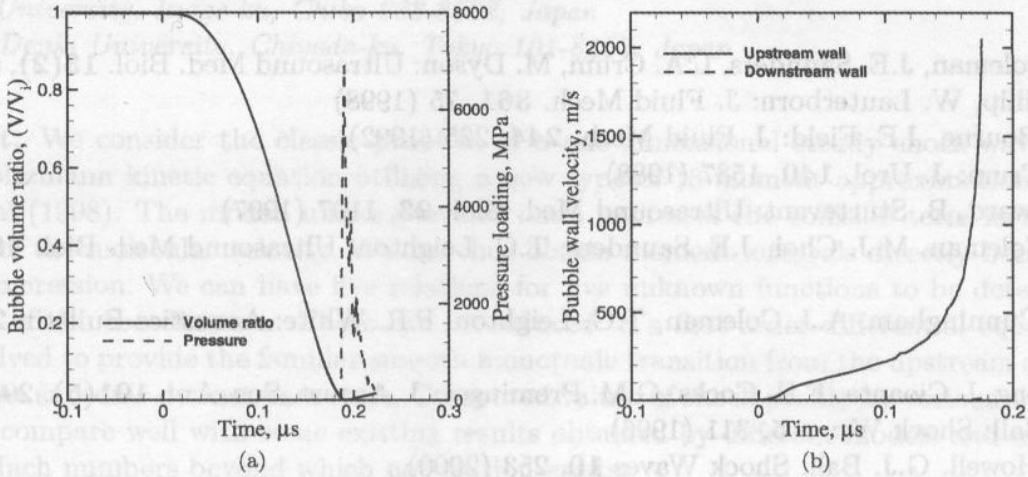

Fig. 3. **(a)** Bubble volume time history and pressure loading measured by transducer on the rigid boundary. **(b)** Bubble wall velocity history

The interaction between the high-momentum liquid jet and the downstream low-momentum water produces a strong vortex flow. In addition, the flow is also redirected radially along the rigid boundary. The strong spherical blast wave propagating to the right impacts on the rigid boundary and is reflected back into the surrounding fluid. The strength of this reflected blast wave is around $1400\,MPa$. Part of it interacts with the remaining cavity and transmit an air shock with magnitude of over $250\,MPa$ (Fig. 2(f)). The air cavity as well as the bubble fragments are drawn into the vortex core that brings the bubble even closer to the solid boundary. The rebound and collapse of this air cavity is expected to cause damage to the nearby solid boundary.

The time history of the cavity volume is shown in Fig. 3(a). The volume reduces linearly with time from $t = 0.1 - 0.18\,\mu s$. Following the linear phase, the rate of change of bubble volume decreases owing to the increase in pressure of the air inside the bubble. The first minimum is achieved at around $t = 0.19\,\mu s$. At this time the internal pressure greatly exceeds that of the surrounding water, and therefore the bubble begins to expand. Our simulation was halted after the first collapse. However it is expected that the bubble will enter an oscillatory state of expansion and collapse before entering a phase of prolonged expansion as it encounters the tensile portion of the lithotripter pulse. This is followed by a series of lower-frequency oscillations [7,12]. This stage of the bubble behaviour will be examined in our future work.

5 Conclusion

The simulation of the near field interaction of a single air bubble with a lithotripter pulse near a rigid boundary, in axisymmetric form, has been performed using the Free-Lagrange code *Vucalm*. The results showed that the method allows sharp capture of the bubble boundary at all times and successfully predicts many details of the shock/bubble interaction. The impact of the shock on the upstream bubble wall causes it to involute and form a jet of liquid. The jet penetrates the interior of the bubble and strikes the downstream wall, generating a strong near-spherical blast wave into the surrounding fluid. It is postulated that the liquid jet and strong spherical

blast wave may assist in the fragmentation of kidney stones during clinical lithotripsy. Further work has been carried out to examine the influence on initial bubble size, shock strength and the *stand-off parameter* on the behaviour of the bubble. However, owing to limited space, this work can not be included in the current paper.

References

1. A.J. Coleman, J.E. Saunders, L.A. Crum, M. Dyson: Ultrasound Med. Biol. **13(2)**, 69 (1987)
2. A. Phillip, W. Lauterborn: J. Fluid Mech. **361**, 75 (1998)
3. N.K. Bourne, J.E. Field: J. Fluid Mech. **244**, 225 (1992)
4. L.A. Crum: J. Urol. **140**, 1587 (1988)
5. D. Howard, B. Sturtevant: Ultrasound Med. Biol. **23**, 1107 (1997)
6. A.J. Coleman, M.J. Choi, J.E. Saunders, T.G. Leighton: Ultrasound Med. Biol. **18(3)**, 267 (1992)
7. K.B. Cunningham, A.J. Coleman, T.G. Leighton, P.R. White: Acoustics Bulletin **26(5)**, 10 (2001)
8. P. Zhong, I. Cioanta, F.H. Cocks, G.M. Preminger: J. Acoust. Soc. Am. **101(5)**, 2940 (1997)
9. G.J. Ball: Shock Waves **5**, 311 (1996)
10. B.P. Howell, G.J. Ball: Shock Waves **10**, 253 (2000)
11. G.J. Ball, B.P. Howell, T.G. Leighton, M.J. Schofield: Shock Waves **10**, 265 (2000)
12. C.C. Church: J. Acoust. Soc. Am. **86(1)**, 215 (1989)